Strojniški vestnik - Journal of Mechanical Engineering 66(2020)10, 581-590
© 2020 Journal of Mechanical Engineering. All rights reserved.
DOI:10.5545/sv-jme.2020.6883
Original Scientific Paper
Received for review: 2020-07-25
Received revised form: 2020-09-14
Accepted for publication: 2020-09-21

Effect of Thermal Barrier Coating on the Thermal Stress of Gas Microturbine Blades and Nozzles

Oscar Tenango-Pirin[1] – Elva Reynoso-Jardón[1] – Juan Carlos García[2,*] –
Yahir Mariaca[1] – Yuri Sara Hernández[3] – Raúl Ñeco[1] – Omar Dávalos[1]
[1] Departamento de Ingeniería Industrial y Manufactura, Universidad Autónoma de Ciudad Juárez, México
[2] Centro de Investigación en Ingeniería y Ciencias Aplicadas, Universidad Autónoma del Estado de Morelos, México
[3] Tecnológico Nacional de México/Campus Pachuca, Pachuca de Soto, Hidalgo, México

Thermal barrier coatings play a key role in the operational life of microturbines because they reduce thermal stress in the turbine components. In this work, numerical computations were carried out to assess new materials developed to be used as a thermal barrier coating for gas turbine blades. The performance of the microturbine components protection is also evaluated. The new materials were 8YSZ, Mg_2SiO_4, $Y_3Ce_7Ta_2O_{23.5}$, and $Yb_3Ce_7Ta_2O_{23.5}$. For testing the materials, a 3D gas microturbine model is developed, in which the fluid-structure interaction is solved using CFD and FEM. Temperature fields and stress magnitudes are calculated on the nozzle and blade, and then these are compared with a case in which no thermal barrier is used. Based on these results, the non-uniform temperature distributions are used to compute the stress levels in nozzles and blades. Higher temperature gradients are observed on the nozzle; the maximum temperature magnitudes are observed in the blades. However, it is found that Mg_2SiO_4 and $Y_3Ce_7Ta_2O_{23.5}$ provided better thermal insulation for the turbine components compared with the other evaluated materials. Mg_2SiO_4 and $Y_3Ce_7Ta_2O_{23.5}$ presented the best performance regarding stress and thermal insulation for the microturbine components.

Keywords: thermal barrier coating, gas microturbine, turbine blade, thermal stress

Highlights

- *An investigation of the effectiveness of novel ceramics for TBC applications is carried out for their use in gas microturbine blades.*
- *The Mg_2SiO_4 and $Y_3Ce_7Ta_2O_{23}$ provided the best performance on thermal insulation under operational environments of the turbine.*
- *The Mg_2SiO_4 and $Y_3Ce_7Ta_2O_{23}$ showed similar thermal and mechanical stress magnitudes on the blades, which were the lowest among the materials studied.*
- *The use of those ceramics led diminishing the temperature and stress developed on the blades, which in turn, enables an increase in the operating life of the turbine.*

0 INTRODUCTION

Gas microturbines (GMT) are small turbomachines that work using gases at high temperatures, with power capacities ranging from 15 kW to 300 kW and offer variable speeds from 30,000 rpm up to 120,000 rpm [1]. They operate with the same operation principle of all the conventional gas turbines; therefore, the efficiency of these devices depends on the gas temperature, which can become higher than 1000 K [2] and [3]. Blades and nozzles of the turbines are subjected to different loads like high temperature, corrosion, centrifugal forces, etc., which could lead to failures [4] and [5]. Regarding high temperature, one of the main drawbacks of GMTs is their small size, which augments heat transfer among their components, leading to failures by burning out or highly stressed zones. Highly stressed zones are often located near the root of the blades as a consequence of non-uniform temperature fields because of sudden changes in geometry and restrictions at the root [6] to [9]. In conventional turbines, in order to cool the blades, internal cooling passages are manufactured; however, this method can not be implemented for microturbines, given the size of such machines [10]. Therefore, the thermal barrier coating (TBC) is used to protect turbine blades and to resist high temperatures environments.

A TBC often has a cover that is composed of three layers: the first is a ceramic topcoat (TC) layer, which has direct contact with hot gases; the second is a bond coat (BC) layer, which offers corrosion resistance; the third is a thermally grown oxide (TGO) layer, which is frequently formed between the TC and BC. Ni-based superalloys are often used as a substrate in gas turbines where TBC provides them with thermal insulation. In this way, TBC allows reducing substrate temperature, prolonging the operation life of the turbine and improving turbine efficiency by increasing its operating temperature [11].

---

*Corr. Author's Address: Universidad Autonoma del Estado de Morelos, Av. Universidad 1001, Cuernavaca, Mor., Mexico, jcgarcia@uaem.mx

The design of proper TBC plays a key role in the operating life of turbine blades; as a consequence, several studies are focused on the study of TBC characteristics. Li et al. [12] studied the thickness of TBC for a gas turbine blade. The materials used were ZrO_2-8 wt% Y_2O_3 (8YSZ) as a TC layer, α-Al_2O_3 as TGO layer and NiCrAlY as a BC layer. TC thickness was varied from 100 µm to 1000 µm. It was observed that when increasing the TC layer thickness, the thermal insulation capability and stress levels within the coatings are enhanced. Radwan & Elusta [13] performed one-dimensional (1D) calculations to assessing a four-TBC layer made of Zirconia. They concluded that the TBC layer allowed reducing the blade temperature, thus enhancing the blade durability. Also, the material influenced the temperature distribution. Thickness optimization of a barrier coating of partially stabilized zirconia (PSZ) of a turbine blade was executed by Sankar et al. [6]. TBC thickness was varied from 100 µm to 800 µm, and they found a critical thickness that occurred when thickness reached 550 µm, where heat transfer rate was the lowest. In other research [14], the temperature distribution and thermal stress field of TBC were obtained by employing a 2D decoupled method. TBC included the BC, TGO and TC, where the TC was made of 8YSZ. Non-uniform temperature fields were obtained, and zones with high stress were detected at the suction and the leading edge of the blade. In another study, it was shown that the impact of foreign object damage (FOD) could cause erosion on blade samples with TBC, and was most dangerous as it becomes perpendicular to the surface [5].

Several materials have been developed to be used as TBC and studies have been performed to compare their effectiveness of substrate protection. In a review of the main materials used as TC and TGO presented by Sahith et al. [15], it was concluded that the most common material used as substrate material and bond coat was nickel-based superalloys. Meanwhile, yttria-stabilized zirconia (YSZ) (7 %) was most commonly used as the topcoat. YSZ appears as one of the best options to thermally protect the substrate blade, given its thermo-physical and mechanical properties, such as low thermal conductivity. Regarding the gas microturbines, YSZ was also the preferred material to be used as TBC [16].

In recent studies, some researchers have proposed new materials to be used as TBC for gas turbine applications. Chen et al. [17] proposed the synthesized forsterite-type Mg_2SiO_4 material as an alternative to zirconia. They showed a comparison with zirconia (8YSZ) in terms of mechanical properties. The new material proved to have a lower thermal conductivity at 1073 K (1.5 W/(mK) and 2.2 W/(mK) for the new material and 8YSZ, respectively) and better thermal-shock resistance than those made of 8YSZ. Other mechanical properties, such as hardness, fracture toughness and Young´s modulus were similar to those of zirconia. Shi-min et al. [18] also introduced two novel ceramics for thermal barrier coatings. The proposed synthesized materials, $Y_3Ce_7Ta_2O_{23.5}$ and $Yb_3Ce_7Ta_2O_{23.5}$, were new rare-earth tantalite oxides with thermal conductivities lower than that of 8YSZ at 1000 K. Beyond this temperature, the new materials showed good stability which makes them appropriate for high-temperature applications. In another study, Yang et al. [19] synthesized high-purity $Dy_{0.02}Gd_{0.025}Yb_{0.025}Y_{0.05}Zr_{0.88}O_{1.94}$ (DZ), $Ti_{0.02}Dy_{0.02}Gd_{0.025}Yb_{0.025}Y_{0.05}Zr_{0.86}O_{1.94}$ (TZ), and the YSZ powder and coating. According to their results, the TZ TBCs could effectively protect the superalloy substrate at 1873 K. Also, the thermal conductivity of the TZ coating was lower than both DZ and YSZ, showing its potential to be used as TBC. However, most of those new materials have been tested under controlled conditions in a laboratory, and their effectiveness under realistic turbine operating conditions need to be considered.

Numerical methods are the preferred tools to predict the thermal and structural fields on blades coated with TBC. Abubakar et al. [20] performed a general review of some methods for predicting residual stress in thermal spray coatings, concluding that some finite element method (FEM) schemes provide results of those stresses reasonably close to experiments; thus, they can be used to predict them in coatings. In contrast, Zhu et al. [7], evaluated the effectiveness of three versions of the k-ϵ turbulence model to predict temperature fields by means of computational fluid dynamics (CFD). The k-ϵ realizable offered the most accurate results when modelling blades with one-layer TBC. Li et al. [12] employed the FEM to design the TBC for a gas turbine blade. They found that thermal insulation was enhanced with the increase of the TC. Also, as mentioned before, Tang et al. [14] carried out a fluid-structure interaction (FSI) coupling method to predict stress fields in a turbine blade. However, their model was restricted to a 2D model. In other works [12] and [21], the uniform temperature on blade surfaces and static blade boundary conditions were used. However, these simplified conditions could drive to imprecise results since temperature fields on blade surfaces, induced by high-temperature combustion gases and the blade, are highly three dimensional and non-uniform.

In this work, a 3D FSI decoupling method of a gas microturbine is carried out to assess novel TBC materials proposed in the technical literature for applications in turbine blades. The coating materials studied are taken from literature: 8YSZ, Mg_2SiO_4, $Y_3Ce_7Ta_2O_{23.5}$ and $Yb_3Ce_7Ta_2O_{23.5}$. To accurately predict the non-uniform temperature fields, stationary guide vanes are taken into account for the numerical domain, giving rise to a single axial passage that includes a static guide vane (nozzle), a rotating blade and their corresponding fluid domains. Results in terms of temperature and stress are discussed to identify the most effective thermal barrier coating for the microturbine.

1 METHODS

1.1 Microturbine Characteristics

The main components of a gas microturbine engine are the expansion microturbine, the combustion chamber and the compressor. The expansion turbine section is referred to here as the microturbine. Computational modelling of an axial gas microturbine is performed using Ansys (Fluent and Mechanical structural). The microturbine geometry is taken from the technical literature [22], which is designed to supply output power of about 29 kW at the rated speed of 76,000 rpm. The microturbine geometry consists of one stage with 17 guide vanes of the stator (nozzle) and 32 rotating blades. Given its axisymmetric geometry, one 3D single passage that includes one nozzle and one blade is constructed for CFD and FEM computations.

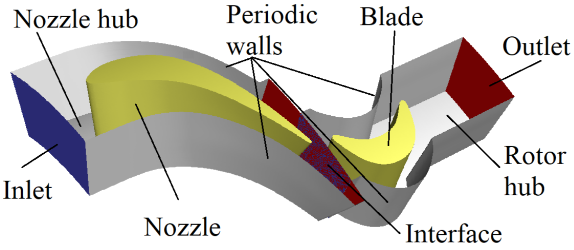

Fig. 1. *Turbine geometry and boundary conditions*

In Fig. 1, the numeric domain is depicted; the shroud is hidden to provide better visualization of the components. The whole computational domain is integrated by both fluid and solid domains corresponding to air and substrate (and TBC) domains. The dimensions of the turbine are 6.82 mm in nozzle height, 7 mm in blade height, 12 mm in nozzle chord, 8 mm in blade chord, and 77.17 mm in maximum turbine diameter.

1.2 Methodology for the CFD and Mesh Characteristics

The numerical domain is discretized to generate the mesh needed for calculations. A mesh dependence analysis is carried out to obtain the optimal mesh for the passage. Given that the nozzle and the rotor domains have meshed separately, an interface boundary condition is used to join both domains. It is noteworthy than both solid and fluid domains been have meshed to predict temperature fields and heat transfer flux. Element sizes of 0.1 mm and 0.2 mm and hexahedral element types are used.

A mesh refinement to model the boundary layer was used in the near-wall region of nozzles and blades. Refinement is defined using 5 to 20 layers with a growth rate of 1.2. As a result, nine different meshes with densities ranging from 1,376,014 to 7,627,342 elements are constructed. After the analysis, a mesh with 6,233,945 (Fig. 2) elements is selected to carry out all computations because it has a variation of about 1 % of the computed substrate temperature with respect to a finer mesh. It should be mentioned that the mesh region corresponding to substrates (nozzles and blades) is used for the FEM solution to solve the stress generation.

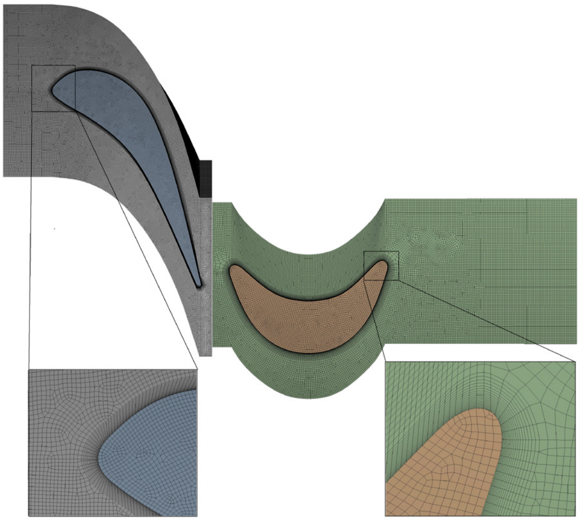

Fig. 2. *Computational mesh for flow field and substrate domains*

1.3 Boundary Conditions of the CFD and Cases of Study

As a consequence of modelling one single passage of the turbine (Fig. 1), boundary conditions are defined as follows: periodic boundary conditions are used at lateral sides of passage, and an interface is created between the nozzle and blade domains to ensure fluid continuity through the passage. The hub and shroud are defined as walls with a no-slip condition. When modelling TBC, thickness and type of material are assigned at coupling walls to model the heat transfer through the coating material. Mass flow rate and pressure outlet conditions are assigned at the inlet and outlet of the passage, respectively. The total mass flow rate incoming to the turbine is equal to 0.23 kg/s at rated speed. Since one single passage is used, this flow rate is divided by the 17 guide vanes resulting in 0.0135 kg/s per passage. The fluid is considered as high-temperature compressible air, and a temperature of 1035 K is also specified at the inlet. The solid domain is defined according to the substrate material (nozzles or blades) and their corresponding TBC.

The investigated TBCs are Mg_2SiO_4, $Y_3Ce_7Ta_2O_{23.5}$ and $Yb_3Ce_7Ta_2O_{23.5}$, which are compared to 8YSZ. Coating material properties are taken from [17] to [19], and their properties are defined based on a temperature range of 973 K to 1073 K to match with the operating temperature of the microturbine. The TBC properties used to predict heat transfer by CFD are indicated in Table 1, which also contains substrate (nozzles and blades) properties [23]. Coating thickness is considered uniform and constant for the whole cases with a value of 550 µm based on some investigations [6] and [12], and it is added as a virtual layer into the CFD software. This virtual technique uses the TBC properties (thermal conductivity, specific heat, density and thickness) to compute heat transfer to the blades.

Table 1. *Top coating and substrate properties*

Material	Thermal conductivity [W/(mK)]	Density [kg/m³]	Specific heat [J/(kgK)]
Nimonic 105 (substrate) [23]	22.23	8010	628
8YSZ [19]	2.2	3610	505
Mg_2SiO_4 [17]	1.76	3210	177000
$Y_3Ce_7Ta_2O_{23.5}$ [18]	1.78	7245	472.1
$Yb_3Ce_7Ta_2O_{23.5}$ [18]	1.4	6321	431.1

1.4 Governing Equations and Turbulence Model

A numerical FSI analysis is conducted using Ansys Workbench commercial code, which is used to solve thermal (Ansys Fluent) and structural (Ansys-Structural) analyses. First, the steady-state Reynolds-averaged Navier Stokes equations (RANS) approach is used to solve governing equations using CFD. Then the FEM is employed to calculate thermal stresses.

CFD is used to compute the flow and temperature fields at steady-state conditions, taking into account the turbine operating conditions, like mass flow, pressure, temperature, wall thermal condition and rotating speed. Governing equations of continuity and momentum, given by Eqs. (1) and (2), are solved using Ansys Fluent. To compute the conjugate heat transfer (CHT), the energy equation, depicted by Eq. (3), is also solved.

$$\frac{\partial \rho}{\partial t} + \left(\rho v_i\right)_i = 0, \tag{1}$$

$$\rho \frac{\partial v_j}{\partial t} + \rho v_{j,i} v_i + p_j - \tau_{ij,i} - \rho F_j = 0, \tag{2}$$

$$\rho \frac{\partial \varepsilon}{\partial t} + \rho \varepsilon_i v_i + p v_{i,i} - \tau_{ij} v_{j,i} + q_{i,i} - \rho r = 0, \tag{3}$$

where t is the time, ρ is the density per unit mass, v_i is the i component of the velocity vector, ε is the internal energy per unit mass, F_i is the i component of the body force vector, p is the pressure, q_i is the heat flux, r is the heat supply per unit mass and τ_{ij} is the viscous stress tensor, respectively, and the comma means is partially derived with respect to the independent variables [24].

As stated before, since the air is considered as compressible, continuity and momentum equations are coupled to the energy equation, which provided the temperature distribution in the flow field. Therefore, in order to solve turbulence and accurately predict the CHT, the realizable $k-\varepsilon$ turbulence model is selected based on the study of Zhu et al. [7]. This model is based on the $k-\varepsilon$ model [25] and differs in the formulation for the turbulent viscosity and for the transport equation for the dissipation rate as follows:

$$\frac{\partial}{\partial t}\left(\rho k\right) + \frac{\partial}{\partial x_j}\left(\rho k u_j\right) = \frac{\partial}{\partial x_j}\left[\left(\mu + \frac{\mu_t}{\sigma_k}\right)\frac{\partial k}{\partial x_j}\right] + G_k + G_b - \rho\varepsilon - Y_M + S_k, \tag{4}$$

$$\frac{\partial}{\partial_t}\left(\rho \varepsilon\right) + \frac{\partial}{\partial x_j}\left(\rho \varepsilon u_j\right) = \frac{\partial}{\partial x_j}\left[\left(\mu + \frac{\mu_t}{\sigma_\varepsilon}\right)\frac{\partial \varepsilon}{\partial x_j}\right] + \rho C_1 S \varepsilon - \rho C_2 \frac{\varepsilon^2}{k + \sqrt{\nu\varepsilon}} + C_{1\varepsilon}\frac{\varepsilon}{k} C_{3\varepsilon} G_b + S_\varepsilon, \tag{5}$$

where $C_1 = \max\left[0.43, \frac{\eta}{\eta + 5}\right]$, $\eta = S\frac{k}{\varepsilon}$, $S = \sqrt{2S_{ij}S_{ij}}$, k is the turbulent kinetic energy and ε is its rate of dissipation. G_k represents the generation of turbulence kinetic energy due to the mean velocity gradients, G_b is the generation of turbulence kinetic energy due to buoyancy, Y_M represents the contribution of the fluctuating compressible turbulence to the overall dissipation rate, C_2, $C_{1\varepsilon}$ and $C_{3\varepsilon}$ are constants, σ_k and σ_ε are the turbulent Prandtl numbers for k and ε, respectively. Finally, S_k and S_ε are user-defined source terms. In contrast, to model the rotation of blades, the multiple reference frame (MRF) model is used. This model is suggested when a steady-state approach is used, and it allows to observe the instantaneous flow field of the moving part as to freezing it. Both stationary and moving domains are governed by continuity and momentum equations (Eqs. (1) and (2)).

To calculate the heat flux transferred from the flow to solid, a conductive and convective problem is modelled by solving the CHT. Newton's law of cooling and Fourier's law are solved to obtain the energy exchange by convection and conduction mechanisms, respectively. Fourier's law to compute the three-dimensional heat conduction is described by Eq. (6):

$$\frac{\partial^2 T}{\partial x^2}+\frac{\partial^2 T}{\partial y^2}+\frac{\partial^2 T}{\partial z^2}+\frac{\dot{q}}{k}=\frac{1}{\alpha}\frac{\partial T}{\partial \tau}, \tag{6}$$

where $\dot{q}$ is the heat transfer rate, k is thermal conductivity, α is the thermal diffusivity of the material, T is the temperature, and x, y and z, are coordinate directions. The convection is solved using Newton law which is given by Eq. (7) as follows:

$$\dot{q}=hA\left(T_w-T_\infty\right), \tag{7}$$

where h is the convection heat-transfer coefficient, A is the surface area, and T_w and T_∞ are the surface and the free stream fluid temperature, respectively. In this case, h is highly influenced by the fluid motion driving to a forced convection case.

In contrast, the thickness of the coating is specified on the walls to obtain the thermal insulation and temperature decrement on turbine components. Temperature fields are needed to calculate stress fields in the blades. Mechanisms for corrosion and erosion, phase transformation of the ceramic coating or its fracture behaviour are neglected to simplify the computations of the effectiveness of thermal insulation of TBCs and the thermal stress induced on nozzles and blades.

1.5 Finite Element Procedure

Once temperature fields are solved using CFD, FEM is employed to compute stress on the components using Ansys Mechanical software. A decoupling method is used, in which the temperature in the components computed by CFD is sent to FEM software. The surface and internal temperature fields of substrates are used as a boundary condition in conjunction with restrictions to elongation of turbine components. Constraints are specified as follows: the nozzle is fixed at the top and bottom surfaces, and the blade is fixed only at its root. The properties of nozzle and blade are assigned based on Nimonic alloy 105 substrate material, as indicated in Table 1. This material is assumed to be homogeneous, continuous, and isotropic. Other properties used are the Young modulus of 139 GPa, the Poisson's Ratio of 0.3 and the thermal expansion coefficient of 15.3×10^{-6}/K [23]. The same solid meshes depicted in Fig. 2 are used to predict three-dimensional stress fields accurately.

1.6 Governing Equations

Thermal stress distribution was calculated following Eqs. (8) to (10); non-uniform and three-dimensional stress fields were obtained. Those equations describe three thermal stress components in the tangential, radial, and longitudinal directions, respectively [26]. The equations allow taking into account partial mechanical constraints and internal constraints due to differences in thermal expansion of elements due to different temperatures. Also, when solving them, it was assumed that thermal equilibrium is reached at the rated speed of the turbine.

$$\sigma_t=\frac{E\alpha}{1-v}\frac{1}{r^2}\left(\frac{r^2+r_i^2}{r_o^2-r_i^2}\int_{r_i}^{r_o}T\cdot rd_r+\int_{r_i}^{r}T\cdot rd_r-T\cdot r^2\right), \tag{8}$$

$$\sigma_r=\frac{E\alpha}{1-v}\frac{1}{r^2}\left(\frac{r^2+r_i^2}{r_o^2-r_i^2}\int_{r_i}^{r_o}T\cdot rd_r+\int_{r_i}^{r}T\cdot rd_r\right), \tag{9}$$

$$\sigma_z=\frac{E\alpha}{1-v}\left(\frac{2}{r_o^2-r_i^2}\int_{r_i}^{r_o}T\cdot rd_r-T\right), \tag{10}$$

where d_r indicates that the definite integrals are solved through the radial direction from inner radius, r_i, to the outer radius, r_o (or an arbitrary intermediate radius, r); E is the Young Modulus, α is the thermal expansion coefficient, v is the Poisson ratio, T is temperature, and t, r, and z are the tangential, radial and longitudinal directions, respectively. Results are represented using the equivalent stress or Von Mises stress, which is derived from the Cauchy stress tensor. The equivalent stress is defined by Eq. (11):

$$\sigma_{eq}=\left(\sigma_t^2+\sigma_r^2+\sigma_z^2-\left(\sigma_t\sigma_r+\sigma_r\sigma_z+\sigma_z\sigma_t\right)\right)^{1/2}, \tag{11}$$

where σ_{eq} is equivalent stress, and t, r, and z are the tangential, radial, and longitudinal directions, respectively. This equivalent stress was taken as the criterion to select the better TBC in terms of the thermal stress generated in the substrate.

2 RESULTS

2.1 Analysis of Temperature Distribution

Analyses of temperature distribution on the components of the whole turbine, with and without TBC, are carried out. For the case of nozzle coated with 8YSZ, the temperature distribution is plotted in Fig. 3. Data show profiles of non-dimensional surface temperature variation at midspan from both pressure and suction sides with non-dimensional blade chord length (Cx). Profiles show that maximum temperature occurs at the trailing edge, then decreases along the substrate forming valleys, and finally, it rises in the leading edge. The trend of temperature is compared with experimental data of Dong et al. [27], and a good agreement is obtained as shown in Fig. 3.

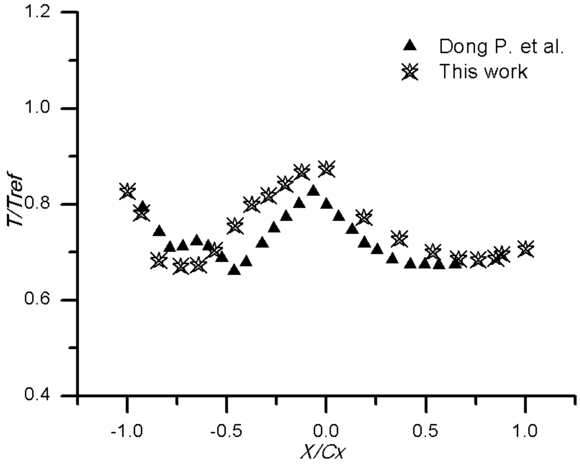

Fig. 3. *Comparison of temperature distribution of vane surface with literature*

The substrate temperature of turbine components is analysed to assess the insulating effectiveness of coating materials. In Fig. 4, the temperature field contours on nozzle and blade without TBC are shown. It can be observed that zones of highest temperature on the nozzle substrate appear at the top of trailing edge (Fig. 4a). Meanwhile, regions of lowest temperature are located at the top of the nozzle and near the middle of the chord line distance where it has its maximum thickness and maximum camber. Also, temperatures on the pressure side are higher than those of the suction side.

In contrast, temperatures of the blade at leading-edge are higher than those of the trailing edge as shown in Fig. 4b, which can be attributed to higher convective heat transfer promoted by gas expansion in this section and blade rotation. Furthermore, a small zone of high temperature is formed at the lower part of the trailing edge near the base of the blade as a consequence of a reduction in blade thickness. The temperature on the blade pressure side is higher than the suction side, where the lowest temperature is identified near the base. According to these results, highly heated zones are detected on the substrates and, with regards to the blade, it reaches temperatures close to the gas temperature. That phenomenon led to the necessity of using TBCs as an insulating method to decrease the temperature and thermal stress in the turbine components.

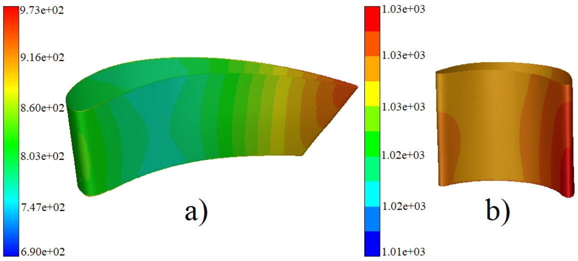

Fig. 4. *Surface temperature in K without TBC; a) nozzle, and b) blade*

Temperature variation with the usage of TBCs is also analysed. The contour plot of surface temperature on turbine components with the TBCs is shown in Figs. 5 and 6. In Fig. 5, surface temperature fields on nozzle are illustrated. The contours reveal a decrease in temperature levels when using TBCs as compared with the case without TBC of Fig. 4a. The temperature distribution between Mg_2SiO_4 and $Y_3Ce_7Ta_2O_{23.5}$ is very similar, and it displays the higher areas of low temperature from all the calculations. However, in the case of $Yb_3Ce_7Ta_2O_{23.5}$, contours show higher temperature than the other TBCs and temperature levels are close to the case without TBC. It can also be observed in Fig. 5 that, even with TBC, the magnitude of temperature at trailing edge is still higher than other zones of the nozzle for all the cases, which is consistent with investigations found in the literature [27] to [29] and the ones shown previously in Fig. 3. Meanwhile, the temperature on the suction side is lower than the pressure side for the whole cases as a consequence of the higher area being protected by the thermal barrier coating and nozzle thickness.

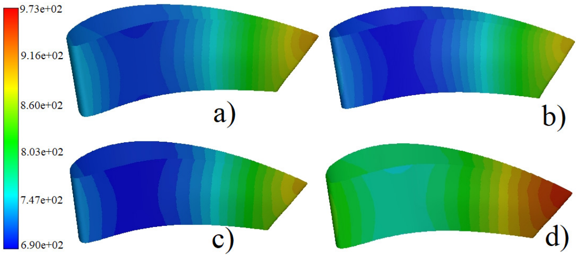

Fig. 5. *Surface temperature of nozzle in K with the coating materials; a) 8YSZ, b) Mg_2SiO_4, c) $Y_3Ce_7Ta_2O_{23.5}$, and d) $Yb_3Ce_7Ta_2O_{23.5}$*

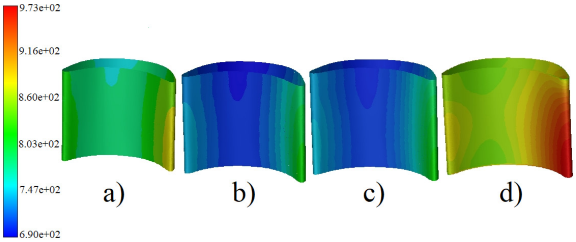

Fig. 6. *Surface temperature of blade in K with the coating materials; a) 8YSZ, b) Mg_2SiO_4, c) $Y_3Ce_7Ta_2O_{23.5}$, and d) $Yb_3Ce_7Ta_2O_{23.5}$*

In contrast, temperature fields developed on the blade are depicted in Fig. 6. Temperature levels are under those obtained from the case without TBC (Fig. 4b). As can be seen from Fig. 6, the temperature on the leading edge is higher than the other regions. Those temperatures are a result of an increase of heat transfer due to the impact of flow with the leading edge driving to the development of a stagnation zone and the decrease of gas velocity. Also, the same small zone of high temperature formed at the lower part of the trailing edge, similar to the case without TBC, can be observed. Regarding thermal insulation, interesting results can be inferred from the contour plots. Temperature distribution between Mg_2SiO_4 and $Y_3Ce_7Ta_2O_{23.5}$ displays the lowest temperatures as it occurs in the nozzle. However, when 8YSZ is applied, temperatures are close to those of $Yb_3Ce_7Ta_2O_{23.5}$. Although these two materials showed the higher temperatures among the TBCs, temperature fields are still lower and distinct to substrate without TBC. Furthermore, similar to the nozzle, $Yb_3Ce_7Ta_2O_{23.5}$ shows the highest temperature among all the coating materials.

To assess the thermal insulation effectiveness of the barrier coatings, maximum and minimum temperature values on the substrates are summarized in Table 2. Data are classified by the turbine component and their corresponding TBC, including the calculation without TBC. Maximum temperatures on each component are located at trailing edge and leading edge for the nozzle and the blade, respectively, as shown before in Figs. 4 and 5. In the nozzle substrate, the maximum and minimum temperatures are obtained with the No TBC and the Mg_2SiO_4 cases, respectively. However, the temperatures between $Y_3Ce_7Ta_2O_{23.5}$and Mg_2SiO_4 cases are very close. The highest of the maximum temperature is 972.6 K, while the lowest value of the maximum temperature is equivalent to 893.5 K. Hence, the drop of temperature, when Mg_2SiO_4 is applied, is about 80.0 K. In contrast, when analysing the blade substrate, the maximum and minimum temperatures also appear when no TBC is used and when Mg_2SiO_4 is assigned, respectively.

Table 2. *Temperature levels on the components with and without TBC*

Material	Temperature [K]			
	Nozzle		Blade	
	minimum	maximum	minimum	maximum
No TBC	779.04	972.64	1022.48	1032.97
8YSZ	704.75	907.79	1018.69	1026.05
Mg_2SiO_4	689.54	893.54	1012.67	1021.87
$Y_3Ce_7Ta_2O_{23.5}$	690.34	894.4	1012.94	1022.01
$Yb_3Ce_7Ta_2O_{23.5}$	771.81	957.24	1023.28	1032.90

Among the maximum temperatures, the peak value is 1032.9 K, and the lowest one is 1021.8 K. As a result, drop of temperature when using Mg_2SiO_4 is a little more of 11 K. This drop of temperature is due to cooling the blade is a hard task owing to high heat transfer rate product of the forced convection of the turbine operation. Other parameters, including gas pressure, temperature or velocity, were not affected at all by the change of TBCs, and they were neglected from analysis of the results. In conclusion, the better thermal insulation on both components is provided by Mg_2SiO_4 and $Y_3Ce_7Ta_2O_{23.5}$ barriers. These results reveal that the thermal protection of these new materials is better than that provided by YSZ.

2.2 Analysis of Stress Distribution

Thermal stress fields are determined by considering temperature obtained by CFD as thermal load in the FEM model using a decoupled method. In Fig. 7, thermal stress distribution on the substrate of components (nozzles and blades) without TBC is illustrated through the Von Mises stress. In the nozzle, maximum stress is gotten at the trailing edge bottom due to the combination of the highest temperature in this region and constraints at the root (Fig. 4a). Some concentration of stress also can be observed at the middle of the chord length and top of the nozzle as a consequence of the temperature gradient. In contrast, the highest stress magnitude on the blade is located at the bottom of the leading edge, as observed in Fig. 7b. Also, high stress can be distinguished at the bottom of the trailing edge. In general, most of the stress of this component is distributed along the base because of the constraints to deformation in this zone. Additionally, the stress in the suction side is higher than the pressure side.

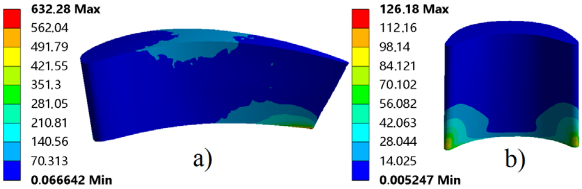

Fig. 7. *Von Mises stress in MPa on the components without TBC; a) nozzle, and b) blade*

Stress distributions on the nozzle substrate when using TBCs are shown in Fig. 8. It can be seen that the distribution of stress is very similar to Fig. 7a when no TBC is used. Maximum stress is also located at the trailing edge, and a stressed zone also appears at the middle chord length of the nozzle for all the cases with TBC. The main differences, however, can be found on stress levels. When 8YSZ is applied, substrates exhibit the highest stress magnitude, which can be attributed to a higher temperature gradient owing to non-uniform inner temperature, as observed in Fig. 5a. Calculations with Mg_2SiO_4, $Yb_3Ce_7Ta_2O_{23.5}$ and $Y_3Ce_7Ta_2O_{23.5}$ indicate a similarity in stress magnitudes.

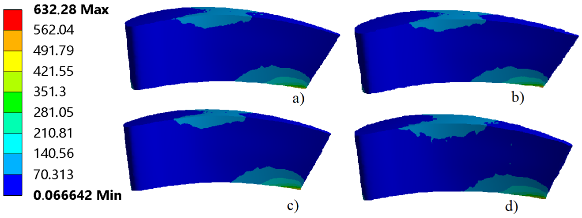

Fig. 8. *Von Mises stress in MPa on the nozzle with TBC; a) 8YSZ, b) Mg_2SiO_4, c) $Y_3Ce_7Ta_2O_{23.5}$, and d) $Yb_3Ce_7Ta_2O_{23.5}$*

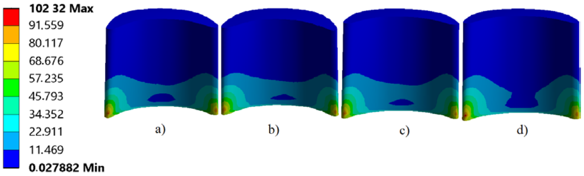

Fig. 9. *Von Mises stress in MPa on the blade with TBC; a) 8YSZ, b) Mg_2SiO_4, c) $Y_3Ce_7Ta_2O_{23.5}$, and d) $Yb_3Ce_7Ta_2O_{23.5}$*

In Fig. 9, Von Mises contour results on the blade substrate are shown for the TBC cases. Distribution of high stress was also similar to Fig. 7b when no thermal protection is used, including the $Yb_3Ce_7Ta_2O_{23.5}$. The four TBCs yielded similar stress distribution inside the blade. Most of the highest stresses are calculated at the leading edge, the trailing edge, and the blade root. Also, stress on the suction side is higher than the pressure side zone. The maximum stress magnitude, however, is under the values obtained when no TBC is used. Hence, these results reveal that all the thermal barriers protect the blade in terms of diminishing the stress generated by the high temperatures and constraints.

3 DISCUSSION

For a better understanding of the effect of the thermal barrier coating on the stress of substrates, the maximum equivalent stress magnitudes from each TBC case are shown in Table 3. It is observed that the maximum stress values on the nozzle substrate when using TBC are close to each other, but they are under yield stress of the material. Among them, the highest stress is produced when using 8YSZ with a stress drop of about 30 MPa. In contrast, the lowest stress values are obtained from the Mg_2SiO_4 and $Y_3Ce_7Ta_2O_{23.5}$ barriers yielding a stress reduction of around 41.0 MPa. However, it should be pointed out that the difference in stress reduction between Mg_2SiO_4, $Y_3Ce_7Ta_2O_{23.5}$ and $Yb_3Ce_7Ta_2O_{23.5}$ is barely observable. Therefore, those three materials provide almost the same stress reduction in the nozzle substrate. In contrast, from Table 3, it can be seen that while temperature decreases in the blade, TBCs stress is also reduced. The maximum stress magnitudes of the substrate are quite similar for all the calculations. The four thermal barriers yield a stress reduction on the blade of around 24 MPa compared with the no TBC case.

Table 3. *Maximum Von Mises stress on the components with and without TBC*

Material	Equivalent stress [MPa]	
	Nozzle	Blade
No TBC	632.28	126.18
8YSZ	601.01	102.58
Mg_2SiO_4	591.40	102.31
$Y_3Ce_7Ta_2O_{23.5}$	591.91	102.32
$Yb_3Ce_7Ta_2O_{23.5}$	593.29	102.41

4 CONCLUSIONS

A 3D model of a microturbine is simulated to assess the effect of TBC on temperature distribution and thermal stress fields on nozzles and blades. Four different thermal barrier coatings materials are tested: 8YSZ, Mg_2SiO_4, $Y_3Ce_7Ta_2O_{23.5}$ and $Yb_3Ce_7Ta_2O_{23.5}$, and compared with a no TBC case. The temperature fields are calculated solving a conjugated heat transfer problem that includes fluid-structure interaction using CFD. The thermal stress distribution is calculated with FEM, using the temperature inside the solid substrates obtained from CFD. The results show a highly three-dimensional and non-uniform temperature distribution on the turbine components, which affected the thermal stress. The maximum temperatures are located at the trailing edge and the leading edge for the nozzle and blade, respectively. The best thermal insulation from both components is obtained with the Mg_2SiO_4 and $Y_3Ce_7Ta_2O_{23.5}$ materials which allow to obtain the highest temperature reduction of substrate. In contrast, when using a TBC to protect the blade substrate, the stress is less affected, producing almost the same magnitudes among the four cases. However, if thermal protection is considered, Mg_2SiO_4 and $Y_3Ce_7Ta_2O_{23.5}$ materials show an advantage over the other thermal barriers to protect the microturbine components. Data obtained with the usage of these new materials provide better results than YSZ, which is currently one of the most materials used for gas turbine applications, regarding temperature reduction and the stress generated.

5 REFERENCES

[1] Nascimento, M.A.R., Rodrigues, L., Santos, E., Gomes, E.E.B., Dias, F.L.G., Velásques, E.I.G., Carrillo, R.A.M. (2013). Micro gas turbine engine: A review, Benini, E. (ed.), *Progress in Gas Turbine Performance*. IntechOpen, London, p. 107-141, **DOI:10.5772/54444**.

[2] Xie, Y., Lu, K., Liu, L., Xie, G. (2014). Fluid-thermal-structural coupled analysis of a radial inflow micro gas turbine using computational fluid dynamics and computational solid mechanics. *Mathematical Problems in Engineering*, vol. 2014, art. ID 640560, **DOI:10.1155/2014/640560**.

[3] Swar, R., Hamed, A., Shin, D., Woggon, N., Miller, R. (2012). Deterioration of thermal barrier coated turbine blades by erosion. *International Journal of Rotating Machinery*, vol. 2012, art. ID 601837, **DOI:10.1155/2012/601837**.

[4] Carter, T.J. (2005). Common failures in gas turbine blades. *Engineering Failure Analysis*, vol. 12, no. 2, p. 237-247, **DOI:10.1016/j.engfailanal.2004.07.004**.

[5] Golewski, P., Sadowski, T. (2019). The influence of TBC aging on crack propagation due to foreign object impact. *Materials*, vol. 12, no 9, art ID 1488, **DOI:10.3390/ma12091488**.

[6] Sankar, V., Ramkumar, P.B., Sebastian, D., Joseph, D., Jose, J., Kurian, A. (2019). Optimized thermal barrier coating for gas turbine blades. *Materials Today: Proceedings*, vol. 11, part 3, p. 912-919, **DOI:10.1016/j.matpr.2018.12.018**.

[7] Zhu, W., Wang, J.W., Yang, L., Zhou, Y.C., Wei, Y.G., Wu, R.T. (2017). Modeling and simulation of the temperature and stress fields in a 3D turbine blade coated with thermal barrier coatings. *Surface and Coatings Technology*, vol. 315, p. 443-453, **DOI:10.1016/j.surfcoat.2017.03.012**.

[8] Guo, J., Xie, D., Zhang, H., Jiang, W., Zhou, Y. (2016). Effect of heat transfer coefficient of steam turbine rotor on thermal stress field under off-design condition. *Frontiers in Energy*, vol. 10, p. 57-64, **DOI:10.1007/s11708-015-0385-3**.

[9] Sadowski, T., Golewski, P. (2015). Cracks path growth in turbine blades with TBC under thermo – mechanical cyclic loadings. *Frattura ed Integrità Strutturale*, vol. 10, no. 35, p. 492-499, **DOI:10.3221/IGF-ESIS.35.55**.

[10] Soares, C. (2011). *Microturbines: Applications for Distributed Energy Systems*. Elsevier, Belington.

[11] Clarke, D.R., Oechsner, M., Padture, N.P. (2012). Thermal-barrier coatings for more efficient gas-turbine engines. *MRS Bulletin*, vol. 37, no. 10, p. 891-898, **DOI:10.1557/mrs.2012.232**.

[12] Li, B., Fan, X., Li, D., Jiang, P. (2017). Design of thermal barrier coatings thickness for gas turbine blade based on finite element analysis. *Mathematical Problems in Engineering*, vol. 2017, art ID. 2147830, **DOI:10.1155/2017/2147830**.

[13] Radwan, M.M., Elusta, S.A. (2016). Thermal barrier coatings for temperature management of gas-turbine blades. International Journal of Research in Chemical. *Metallurgical and Civil Engineering*, vol. 3, no. 2, p. 219-222, **DOI:10.15242/ijrcmce.iae0716412**.

[14] Tang, W.Z., Yang, L., Zhu, W., Zhou, Y.C., Guo, J.W., Lu, C. (2016). Numerical simulation of temperature distribution and thermal-stress field in a turbine blade with multilayer-structure TBCs by a fluid–solid coupling method. *Journal of Materials Science & Technology*, vol. 32, no. 5, p. 452-458, **DOI:10.1016/j.jmst.2016.03.009**.

[15] Sahith, M.S., Giridhara, G., Kumar, R.S. (2018). Development and analysis of thermal barrier coatings on gas turbine blades – a review. *Materials Today: Proceedings*, vol. 5, no. 1, p. 2746-2751, **DOI:10.1016/j.matpr.2018.01.060**.

[16] Naraparaju, R., Lau, H., Lange, M., Fischer, C., Kramer, D., Schulz, U., Weber, K. (2018). Integrated testing approach using a customized micro turbine for a volcanic ash and CMAS related degradation study of thermal barrier coatings. *Surface and Coatings Technology*, vol. 337, p. 198-208, **DOI:10.1016/j.surfcoat.2018.01.030**.

[17] Chen, S., Zhou, X., Song, W., Sun, J., Zhang, H., Jiang, J., Deng, L., Dong, S., Cao, X. (2019). Mg2SiO4 as a novel thermal barrier coating material for gas turbine applications. *Journal of the European Ceramic Society*, vol. 39, no. 7, p. 2397-2408, **DOI:10.1016/j.jeurceramsoc.2019.02.016**.

[18] Shi-min, W., Wei-wei, Z., Hong-song, Z., Fei, W., Debing, S., Xian-feng, Y., Zhi-he, S., Qun-peng, D., Wen-peng, M. (2019). $Y_3Ce_7Ta_2O_{23.5}$ and $Yb_3Ce_7Ta_2O_{23.5}$—two kinds of novel ceramics for thermal barrier coatings. *Ceramics International*, vol. 45, no. 8, p. 10414-10419, **DOI:10.1016/j.ceramint.2019.02.100**.

[19] Yang, M., Zhu, Y., Wang, X., Wang, Q., Ai, L., Zhao, L., Chu, Y., Guo, S., Hu, J., Zhang, Q. (2019). Preparation and thermophysical properties of Ti^{4+} doped zirconia matrix thermal barrier coatings. *Journal of Alloys and Compounds*, vol. 777, p. 646-654, **DOI:10.1016/j.jallcom.2018.11.034**.

[20] Abubakar, A.A., Arif, A.F.M., Al-Athel, K.S., Akhtar, S.S., Mostaghimi, J. (2017). Modeling residual stress development in thermal spray coatings: Current status and way forward. *Journal of Thermal Spray Technology*, vol. 26, p. 1115-1145, **DOI:10.1007/s11666-017-0590-1**.

[21] Yang, L., Liu, Q.X., Zhou, Y.C., Mao, W.G., Lu, C. (2014). Finite element simulation on thermal fatigue of a turbine blade with thermal barrier coatings. *Journal of Materials Science & Technology*, vol. 30, no. 4, p. 371-380, **DOI:10.1016/j.jmst.2013.11.005**.

[22] Tenango-Pirin, O., Garcia, J.C., Castro-Gomez, L., Rodriguez, J.A., Sierra, F., De Santiago, O., Rodriguez-Lelis, J.M. (2016). Effect of the modification of the start-up sequence on the thermal stresses for a microgas turbine. *International Journal of Rotating Machinery*, vol. 2016, art. ID 5834172, **DOI:10.1155/2016/5834172**.

[23] NIMONIC® alloy 105 (2007) from: *https://www.specialmetals.com/assets/smc/documents/alloys/nimonic/nimonic-alloy-105.pdf*, accessed on 2019-10-24

[24] Chung, T. (2010). *Computational Fluid Dynamics*. Cambridge university press, Cambridge.

[25] Launder, B.E., Spalding, D.B. (1974). The numerical computation of turbulent flows. *Computer Methods in Applied Mechanics and Engineering*, vol. 3, no. 2, p. 269-289, **DOI:10.1016/0045-7825(74)90029-2**.

[26] Kim, T.S., Lee, D.K., Ro, S.T. (2000). Analysis of thermal stress evolution in the steam drum during start-up of a heat recovery steam generator. *Applied Thermal Engineering*, vol. 20, no. 11, p. 977-992, **DOI:10.1016/S1359-4311(99)00081-2**.

[27] Dong, P., Wang, Q., Guo, Z., Huang, H., Feng, G. (2009). Conjugate calculation of gas turbine vanes cooled with leading edge films. *Chinese Journal of Aeronautics*, vol. 22, no. 2, p. 145-152, **DOI:10.1016/S1000-9361(08)60080-1**.

[28] Wang, Z., Yan, P., Guo, Z., Han, W. (2008). BEM/FDM conjugate heat transfer analysis of a two-dimensional air-cooled turbine blade boundary layer. *Journal of Thermal Science*, vol. 17, p. 199-206, **DOI:10.1007/s11630-008-0199-2**.

[29] Rezazadeh Reyhani, M., Alizadeh, M., Fathi, A., Khaledi, H. (2013). Turbine blade temperature calculation and life estimation - a sensitivity analysis. *Propulsion and Power Research*, vol. 2, no. 2, p. 148-161, **DOI:10.1016/j.jppr.2013.04.004**.